

Detectability of gravitational higher order modes in the 3G era

Divyajyoti,^{1,*} Preet Baxi,^{1,†} Chandra Kant Mishra,^{1,‡} and K. G. Arun^{2,§}

¹*Indian Institute of Technology Madras, Chennai, 600036, India*

²*Chennai Mathematical Institute, Siruseri, 603103, India*

(Dated: March 13, 2022)

Detection of higher order modes of gravitational waves in third-generation ground-based detectors such as Cosmic Explorer and Einstein Telescope is explored. Assuming an astrophysical population of binary black holes based on events reported in the second gravitational wave catalog by LIGO and Virgo (GWTC-2), we assess the detectability of these higher order modes using a network consisting of three third-generation detectors. We find that the two sub-leading modes ((3,3) and (4,4)) can be detected in around 80% of the population with a network signal-to-noise ratio of 10 or more, and for nearly 20% of the sources, all six leading modes will be detectable. Besides, a study concerning the effect of binary's mass ratio and its orbital inclination with the observer's line-of-sight in detecting various modes is presented. For a few selected events of the LIGO-Virgo catalog, we identify the modes that would have been detected if a third-generation detector was operational when these events were recorded. Observing these higher order modes in the 3G era would have a huge impact on the science possible with these detectors ranging from astrophysics and cosmology to testing strong-field gravity.

I. INTRODUCTION

Since the discovery of the first gravitational wave (GW) event [1] in 2015, LIGO Scientific Collaboration and Virgo collaboration have reported the detection of a total of 47 compact binary mergers with false alarm rate (FAR) $< 1\text{yr}^{-1}$ [2]. These include 44 binary black hole (BBH), two binary neutron star (BNS), and one possible neutron star-black hole (NSBH) mergers. Additionally, independent analyses using the publicly available data [3] have confirmed these detections and have also added a few marginal BBH events to the LIGO-Virgo catalog [4–8]. These observations have provided us with several new insights into astrophysics, cosmology, and fundamental physics (see for instance, Refs. [9–13]).

The two advanced LIGO (aLIGO) detectors [14] in the US and advanced Virgo [15] in Europe participated in the first two observing runs (named, O1 and O2), as well as for the first half of the third observation run (O3a). The Japanese detector KAGRA [16] joined the LIGO-Virgo network briefly towards the end of the third observing run. The second part of the third observing run (O3b) was concluded in March 2020.

While existing detectors are being upgraded towards LIGO A+ design [17, 18], beyond A+ upgrades (LIGO Voyager [18]) and the next-generation detector configurations [19, 20] have already been proposed and science studies are currently ongoing. Cosmic Explorer (CE) [18, 20, 21] and Einstein Telescope (ET) [19, 22] are two leading third-generation (3G) detector proposals. Both are expected to have a strain sensitivity that is an order

of magnitude better than the second-generation (2G) detectors such as aLIGO and aVirgo, and a low-frequency cutoff in the range of 1-5 Hz [23].

While BBH mergers are already the most frequently detected GW events [2], they are also among the strongest emitters of GWs and are possibly the cleanest¹ ones to model using analytical and numerical techniques in general relativity (GR) [24]. If the gravitational waveforms are known precisely, one can use a well known data-analysis technique called *matched filtering* [25] to extract signals from noisy detector output. The method involves cross-correlating the detector data with an accurate set of templates that closely mimic the form of expected signals and are computed in advance. The success of the method critically depends on how accurate these model predictions are. This requirement has driven the signal-modeling efforts over the past four decades by the gravitational wave community across the globe [26–32].

The exact form of the signal depends on several intrinsic and extrinsic source parameters. Hence it is important that its theoretical predictions (templates) include all possible effects, neglect of which can potentially induce systematic biases in the measurement of source parameters or worse can even lead to non-detection of these signals. One such effect is the presence of non-quadrupole modes (also referred to as subdominant modes or higher order modes) in signals from compact binary systems which are asymmetric (unequal mass components) and/or whose orbital planes are not optimally inclined towards the Earth (face-off binaries). The effect of non-quadruple modes on the detection and parameter estimation for binary black holes have been studied extensively (see for instance Refs. [33–38]) and

*Electronic address: divyajyoti@physics.iitm.ac.in

†Electronic address: pbaxi1199@gmail.com

‡Electronic address: ckm@physics.iitm.ac.in

§Electronic address: kgarun@cmi.ac.in

¹Near monochromatic GW signals from isolated neutron stars too can be modeled very accurately in GR and with relative ease.

have now been included in a number of models that have been obtained by performing fits to Numerical Relativity simulations (see for instance, Refs. [39–43]), or following the effective-one-body approach (see Refs. [44, 45]).

A. Implications of higher order modes

One of the most important consequences of including higher order modes into the gravitational waveforms can be linked to their sensitivity to frequencies that are inaccessible through the dominant (quadrupole) mode. Typically, including higher order modes into the waveforms will extend the GW spectrum to higher frequencies. For instance, inspiral for the dominant (quadrupole) mode ($\ell=2$, $m=2$ or simply the 22 mode) can be assumed to terminate at twice the orbital frequency at the last stable orbit (f_{LSO}), while the same for a higher mode waveform including the k^{th} harmonic will be visible until the GW frequency becomes $k f_{\text{LSO}}$. The direct consequence of this is the increase in the mass reach of broadband detectors [46, 47].

The higher order modes, through amplitude corrections to gravitational waveforms, also bring in new dependencies in terms of the mass ratio, component spins, and inclination angle into the gravitational waveforms; see for instance Ref. [48] (non-spinning case), and [49] (for spinning case). By including them into the waveforms, one is able to break the degeneracies present in the waveform, such as those between inclination angle and luminosity distance [50], and that between mass ratio and spins [51, 52]. This proves to be a very useful tool when extracting source properties and finds numerous implications in astrophysics [34–36, 48, 53–66], cosmology [53, 55, 67] and fundamental physics [63, 64]. For instance, inclusion of higher modes breaks the distance-inclination angle degeneracy, allowing for their improved measurements. While better distance measurements of the luminosity distance allow putting tighter bounds on cosmological parameters such as the Hubble constant [67, 68], improved inclination angle estimates can lead to better modeling of off-axis Gamma Ray Bursts (GRBs) [56].

Further, the use of higher modes has been shown to improve the efficiency of parameterized tests of GR [69, 70] and massive graviton tests [71]. A new test of GR based on the consistency of different modes of the gravitational waveform was proposed [63, 72, 73] and performed on a few selected events from the O3a [74]. A multipolar null test of GR was also proposed in Refs. [75, 76] which would measure the contribution to the gravitational waveforms from various multipoles and test their consistency with the predictions of GR. Recently, it was shown that detection of higher modes can improve the early warning time and localization of compact binary mergers, especially NS-BH systems [77, 78].

B. Detection of higher modes by LIGO/Virgo

It should be clear from the discussion above that higher order modes become relevant when the binary is not face-on and/or its components have very different masses. Additionally, the multipolar structure of the radiation field guarantees relatively weaker strengths of higher order modes compared to the dominant quadrupole mode. In other words, we are more likely to detect quadrupolar mode from near equal-mass/face-on binary compared to non-quadrupole modes from an unequal mass/face-off system. This detection bias makes it difficult to detect higher order modes in observed sources. It was only recently that LIGO/Virgo observations showed the presence of these modes in an unambiguous way. While there was a hint of higher mode presence in the data for the event GW170729 [62], clear evidence of a higher order mode was found during the analysis of two events namely, GW190412 [65] and GW190814 [66] both highly asymmetric in component masses. Further, for about six events (all observed during the first part of the third observing run of the LIGO-Virgo network), the inclusion of higher modes in waveform models was found to improve the parameter estimation accuracies [2, 79], hinting at their presence.

C. Motivation for the present work

As ground-based detectors improve their sensitivities over the next few years, they are going to detect more massive and more distant BBHs, should they exist. The increased mass reach is mostly due to the improved lower cut-off frequency of these detectors which may be as low as a few Hz.² The increased distance reach is due to the improved sensitivity at different frequency bands. Going by the present estimates, these observations would definitely unravel more asymmetric binary systems many of which may not be face-on. This should facilitate detections of several of the sub-dominant modes by the next-generation detectors. As these higher modes would very likely bring in improvements to the parameter estimation in various contexts, a study of their detectability is a very important first step towards understanding the impact they will have on GW science. This forms the context of the present work where we quantify the detectability of non-quadrupolar modes using a network of future ground-based gravitational wave detectors.

Our study on a third-generation (3G) detector network, using quasi-circular, non-precessing higher mode waveforms [41], finds that about 80% of the population will detect the two sub-leading modes, $\ell=3$, $m=3$ (or simply the 33 mode) and $\ell=4$, $m=4$ (or 44 mode) mode, in

²Note that inclusion of higher modes also improves detector’s mass reach as discussed above in Sec. IA.

addition to the dominant 22 mode. Further, for about 20% population, it is possible to detect all the six leading spherical harmonic modes (*i.e.* 22, 21, 33, 32, 44, and 43). These should have a profound impact on the planned astrophysics, cosmology, and fundamental physics using these detectors.

The layout of the paper is as follows. Section II includes details of the waveform employed and our choice of detector network(s) used in the analysis. We start Sec. III by discussing the detection criteria (used throughout the paper) followed by results of a study concerning the detectability of higher order modes in the mass ratio (q) and inclination angle (ι) plane. Additionally, detection of higher modes in selected GWTC-2 events, assuming a 3G detector was operational during the O3a run of LIGO and Virgo, is explored. Section IV presents the results of a full population study (based on the observed BBH population reported in [2]) using a 3G detector network, along with a comparison study with a network of 2G detectors and their future upgrades.

II. WAVEFORMS AND DETECTOR NETWORKS

A. Spin-weighted spherical harmonic basis and the higher mode waveform structure

Multipolar decomposition of the gravitational waveform is a convenient tool to represent the gravitational radiation from systems like compact binary mergers [80] and helps immensely in handling the nonlinearities of GR in the perturbative approaches to GR such as PN theory (see Ref. [26] for a detailed review). Symmetric trace-free tensors and spin-weighted spherical harmonics provide two equivalent bases for such a decomposition (see for instance Refs. [81, 82]). The latter has been more popular recently due to the extensive use of it by the numerical relativity community, as it provides a natural basis for extracting the waveform from numerical simulations (see for instance Ref. [83]).

The GW strain can be expressed as a linear combination of different modes defined using a basis of spin-weighted spherical harmonics of weight -2 as follows [84]

$$h(t, \vec{\lambda}, \Theta, \Phi) = \sum_{\ell \geq 2} \sum_{-\ell \leq m \leq \ell} h^{\ell m}(t, \vec{\lambda}) Y_{-2}^{\ell m}(\Theta, \Phi). \quad (1)$$

Here, t denotes the time coordinate, the intrinsic parameters like masses and spins are denoted by $\vec{\lambda}$, and (Θ, Φ) are the spherical angles in a source-centered coordinate system with total angular momentum along the z -axis. A number of waveforms, both numerical and phenomenological, have been developed which include higher modes [39–45, 85–96]. Many of these waveforms are incorporated in the LSC Algorithm Library Suite (LALSuite) [97]. These waveforms make use of the analytical and semi-analytical treatment of the compact binary

dynamics within the PN [71, 82, 98–115] and Effective One Body [30, 116–121] frameworks as well as of numerical relativity (NR) simulations (see Ref. [122] for a recent update on NR waveform catalog by the SXS collaboration and Ref. [123] by the Georgia Tech group, both catalogs are publicly available; see also [124]). A comparison between different numerical relativity schemes leading to simulations of BBH spacetimes can be found in Refs. [125, 126].

For our study, we choose to work with an inspiral-merger-ringdown waveform model of Phenom family for BBHs in quasi-circular orbits including the effect of higher order modes and non-precessing spins (coded up in LALSuite with the name IMRPhenomHM) [41]. In addition to the dominant 22 mode this model can be used to extract other sub-dominant gravitational wave modes (21, 33, 32, 44, and 43) and is calibrated for the mass ratios ($q = m_1/m_2$; $m_1 > m_2$) up to 18, and component dimensionless spin magnitudes up to 0.85 (up to 0.98 for equal mass case) [see [41] for details].

B. Detector networks

For our study, we consider network(s) consisting of two kinds of 3G detectors: Cosmic Explorer (CE) and Einstein Telescope (ET). Cosmic Explorer (CE) will be similar in layout to the current LIGO detectors, with two arms at a right angle to each other, forming an L-shape. The length of these two arms is proposed to be 40 km each, which is 10 times longer than the advanced LIGO detector. Einstein telescope (ET), on the other hand, will have a different layout. It will consist of three arms forming an equilateral triangle. Each arm will have a length of 10 km, and the whole setup is underground. Both detectors are expected to achieve a sensitivity that is roughly an order of magnitude better than the current 2G detectors (aLIGO), on average, and a low-frequency sensitivity in the range 1-5 Hz [23].

Further, we also compare the detection of higher modes in the 3G network with that in the upgraded 2G networks with LIGO A+ configuration [17, 18] and LIGO Voyager [18]. Both LIGO A+ and LIGO Voyager are expected to have an overall improved sensitivity compared to that of current generation detectors (see Fig. 1).

While the investigations presented in Sec. III are in the context of a single 3G configuration (Cosmic Explorer (CE)), a three-detector network of 3G detectors is used in the analyses presented in Sec. IV. Our primary 3G network consists of a detector with CE configuration in the US (LIGO-Livingston site), a detector with ET design in Europe (at the Virgo site), and another CE detector in Australia. We refer to this network as the LAE network of 3G detectors. Additionally, three different 3-detector networks have been used to study the detectability of higher order modes as detectors evolve through LIGO A+, LIGO Voyager, and CE configurations. The sensitivity curve [128] and locations of these detectors are

Label	Location	Latitude	Longitude	Orientation	Type(s)
L	Louisiana, USA	0.53	-1.58	-1.26	CE/A+/Voyager
H	Washington, USA	0.81	-2.08	-2.51	CE/A+/Voyager
V	Cascina, Italy	0.76	0.18	2.8	CE/A+/Voyager
A	New South Wales, Australia	-0.59	2.53	0.78	CE
E	Cascina, Italy	0.76	0.18	2.8	ET

Table I: The detector locations which have been used in this study [127]. All angle values are in radians. Some of these sites have not been finalized yet and have been planned/proposed for future detectors.

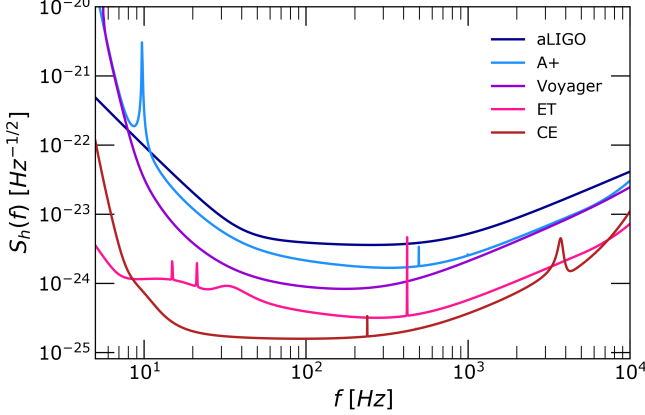


Figure 1: Detector sensitivity curves for various detectors considered in this analysis. In addition, sensitivity for aLIGO is also shown for comparison.

shown in Figure 1 and Table I, respectively. For each detector, we put the lower frequency bound (f_{low}) as 5 Hz following Chamberlain *et al.* [23].³

III. DETECTABILITY OF HIGHER MODES IN 3G DETECTORS

A. Detection criteria

A robust method to quantify confident detection of a weak gravitational wave signal in noisy detector data involves computing the signal-to-noise ratio (SNR). Assuming, a gaussian noise, and that template (signal model) is exactly the same as the signal in the detector data, one can define the ‘optimal’ SNR (ρ) [24, 129, 130] as

$$\rho^2 = (h|h), \quad (2)$$

where $(\cdot|\cdot)$ denotes the noise weighted inner product and h represents the GW strain given by Eq. (1).

³Note that, in Ref. [23], authors have used a low-frequency cut-off of 1Hz for ET configuration, however, we work with a universal low-frequency cutoff of 5Hz for all detector configurations (LIGO A+, LIGO Voyager, CE or ET) in this work.

For any two functions a and b , the inner product is defined as

$$(a|b) = 2 \int_0^\infty \frac{\tilde{a}^*(f) \tilde{b}(f) + \tilde{a}(f) \tilde{b}^*(f)}{S_h(f)} df, \quad (3)$$

where, $\tilde{a}(f)$ represents Fourier transform of the function a . In the above, $S_h(f)$ denotes the power spectral density (PSD) of the detector noise and is a measure of noise in the detector (see Figure 1 for its shape in different detector configurations). Following the definition of optimal SNR (given by Eq. (2)), we can quantify the power in higher order modes by defining the optimal SNR tied to individual modes. We define

$$\rho_{\ell m}^2 = (h_{\ell m}|h_{\ell m}) = 4 \int_0^\infty \frac{|\tilde{h}_{\ell m}(f)|^2}{S_h(f)} df, \quad (4)$$

where $\tilde{h}_{\ell m}(f)$, analogous to the GW strain in frequency domain, represents strain for any $(\ell, \pm m)$ mode pair and can be expressed as a linear combination of associated polarizations, $\tilde{h}_+^{\ell m}(f)$ and $\tilde{h}_\times^{\ell m}(f)$, as

$$\tilde{h}_{\ell m}(f) = F_+(\theta, \phi, \psi) \tilde{h}_+^{\ell m}(f) + F_\times(\theta, \phi, \psi) \tilde{h}_\times^{\ell m}(f) \quad (5)$$

where the antenna pattern functions $F_+(\theta, \phi, \psi)$ and $F_\times(\theta, \phi, \psi)$ are functions of two angles (θ, ϕ) giving binary’s location in sky and the polarisation angle (ψ) . The two polarizations associated with each $(\ell, \pm m)$ mode pair $(\tilde{h}_+^{\ell m}(f), \tilde{h}_\times^{\ell m}(f))$ can suitably be expressed using a basis of spin-weighted spherical harmonics of weight -2 in frequency domain as (see Appendix C of Ref. [39] for details and the derivation)

$$\begin{aligned} \tilde{h}_+^{\ell m}(f) &= \left[(-)^\ell \frac{d_2^{\ell, -m}(\iota)}{d_2^{\ell m}(\iota)} + 1 \right] Y_{-2}^{\ell m}(\iota, \varphi_0) \tilde{h}_{\ell m}^R(f) \\ \tilde{h}_\times^{\ell m}(f) &= -i \left[(-)^\ell \frac{d_2^{\ell, -m}(\iota)}{d_2^{\ell m}(\iota)} - 1 \right] Y_{-2}^{\ell m}(\iota, \varphi_0) \tilde{h}_{\ell m}^R(f) \end{aligned} \quad (6)$$

where $\tilde{h}_{\ell m}^R(f)$ represents the Fourier transform of the real part of the $h_{\ell m}(t)$ appearing in Eq. (1), $d_2^{\ell, m}(\iota)$ are the Wigner d functions and $Y_{-2}^{\ell, m}(\iota, \varphi_0)$ are spin

weighted spherical harmonics of weight -2 (see for example, Ref. [131]).⁴ Note that $\tilde{h}_{\ell m}^R(f)$ can be expressed in terms of an amplitude and a phase associated with each mode as

$$\tilde{h}_{\ell m}^R(f) = A_{\ell m}(f) e^{i\varphi_{\ell m}(f)}, \quad (7)$$

where, $A_{\ell m}(f)$ and $\varphi_{\ell m}(f)$ are obtained in frequency domain by performing fits to a set of target waveforms chosen appropriately (see for instance Ref. [39]). Details and the explicit expressions for the amplitude and the phase models used in this work can be found in Eqs. (4)-(9) of [41].

This definition of mode SNR (given by Eq. 4) closely follows the one in Ref. [132] which was used for quantifying the SNR of the 33 mode for GW190814 [66] and GW190412 [65]. Other methods used for detecting the presence of higher modes have been discussed in [133–135]. For our purposes, we choose to work with a fixed SNR threshold of 10 for individual modes ($\rho_{\ell m}$) defined above. This would mean that a confident detection of a mode requires the corresponding SNR to be above 10. Note however, this may be a little too stringent for some of the higher order modes, search for whose presence may be carried out in conjunction with the 22 mode and therefore may require a lower threshold on SNR. Hence, in order to give the reader the flexibility to interpret the detectability with lower thresholds, our important results show all the events up to an SNR of 5.

It is important to note that the observed gravitational waveform is a superposition of different spherical harmonic modes, and hence the total SNR would contain contributions from the *interference* terms between different harmonics [47, 48]. They are likely to contribute negligibly to the total SNR, compared to the dominant contributions (given by Eq. (4)) as shown in [132] in the context of aLIGO detectors. Regardless of the magnitude of the interference terms, Eq. (4) should be seen as a definition of SNR in different modes.

For all practical purposes we can choose to work with a low and high frequency cut-off ($f_{\text{low}}, f_{\text{cut}}$) and re-express the optimal SNR for each mode as

$$\rho_{\ell m}^2 = 4 \int_{f_{\text{low}}}^{f_{\text{cut}}} \frac{|\tilde{h}_{\ell m}(f)|^2}{S_h(f)} df. \quad (8)$$

As discussed above we choose a universal lower frequency cut-off of 5Hz following Ref. [23]. The high frequency cut-off (f_{cut}) though is decided by the mass of the binary and chosen automatically by waveform module with high enough value so as to not lose any signal power [41].

B. Higher modes in the $q - \iota$ plane

Now that we have a formal definition for the optimal SNR for any mode, and have established a detection criterion, in the sections that follow we shall present the result of our investigations. One of the first things that we intend to discuss here concerns the detection of various sub-dominant modes in the $q - \iota$ plane. Recall, the discussion in Sec. I that these modes not only become relevant when binary has mass asymmetry ($q > 1$) and is not optimally inclined, ($\iota \neq 0$) but might also be detected frequently by the next generation detectors such as those in the 3G era. Hence, quantifying the detectability of higher modes in the $q - \iota$ plane is very important with regard to the physics that is associated with the compact binary mergers. This section focuses on exploring the parameter space in the $q - \iota$ plane which will be accessible through higher order modes in the 3G era. The results of this investigation are summarized in Fig. 2.

The analysis here considers the SNR corresponding to a single detector: CE placed at the location L (refer Table I). Binaries, which act as representative systems, have a fixed value of dimensionless spin components as $\chi_{1z}=0.9$ and $\chi_{2z}=0.8$ and are assumed to be kept at a distance of 1 Gpc, with sky location and polarization angles as $\theta = 30^\circ$, $\phi = 45^\circ$, and $\psi = 60^\circ$, a choice, that though is arbitrary, has no impact on the conclusions.

Figure 2 shows the fixed SNR contours for various higher order modes in the $q - \iota$ plane. Each contour corresponds to the fixed (single detector) SNR of 10 and the region inside each contour has an SNR higher than 10. Contours corresponding to different choices of total mass are displayed in the plot. The contours provide the regions in the $q - \iota$ plane where detection of different sub-dominant modes will be plausible. In other words, any source which lies inside the contours will be detectable, whereas those which lie outside will not be detectable. We observe that while the detection of 33 mode is possible for masses as low as $25M_\odot$, 44 mode can only be detected in heavier systems as displayed by contours in the bottom left panel of Fig. 2. This is not surprising since the 44 mode (compared to the 33 mode) is more sensitive to high frequencies. As heavier systems merge at lower frequencies, they bring the higher mode content to the sweet spot of the detector band allowing the accumulation of SNR. Note also, for a given binary the 44 mode amplitudes are relatively lower than the 33 amplitude and more or less increases linearly with its total mass. This naturally affects the power in a given mode and can explain the non-detection of 44 mode in lighter systems. Similar arguments (based on the frequency sweep of each mode in the detector's band and their relative amplitude) can be outlined to explain the trends seen in Fig. 2 w.r.t. the minimum mass for which a certain mode is detected.

The trends in mass ratio and inclination angle are distinct for each mode. For a particular total mass value, as q increases, we see that the contours become narrower until they close at a point. Any binary with a mass ratio

⁴In writing Eq. (6) we have set for the spherical angles appearing in Eq. (1), $(\Theta, \Phi) \equiv (\iota, \phi_0)$, where ι is binary's inclination angle and ϕ_0 is a reference phase.

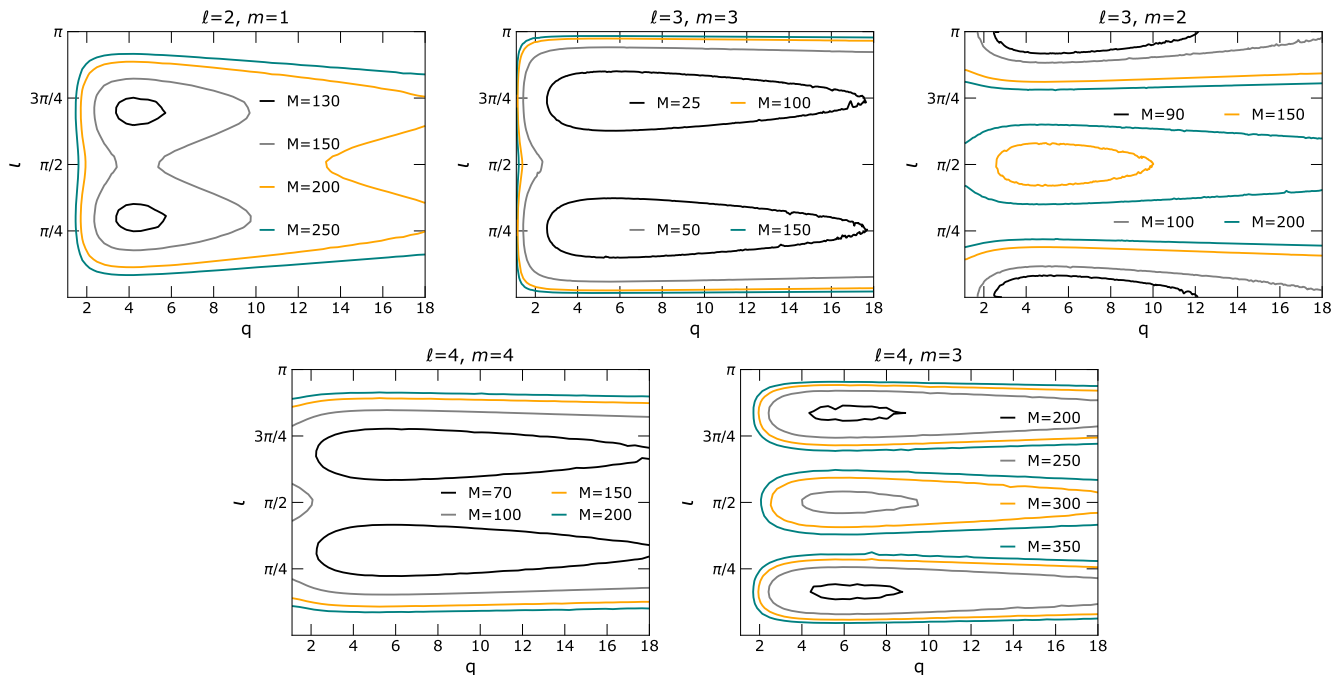


Figure 2: Figure shows fixed SNR ($=10$) contours for various non-quadrupole modes, corresponding to different total mass systems in the $q - \iota$ plane. Each plot corresponds to a particular mode (see panel title). In a particular plot, the contours correspond to different values of total mass. The spin values for all the systems have been taken as $\chi_{1z}=0.9$, $\chi_{2z}=0.8$.

value higher than this point will not be detectable. The maximum mass ratio for detectable binary is very different for each mode. For a total mass of $150 M_{\odot}$, the mass ratio reach of 33, 44, and 32 modes is well beyond 18, whereas for 21 mode it is only up to 10, and for 43 mode, the binary is not even detectable. We can see these distinct (and somewhat complimentary) trends in ι as well. Again, for a total mass of $150 M_{\odot}$, and a fixed mass ratio (say 4), 33 mode covers almost the entire ι range whereas for 44 mode it is somewhat restricted. For 21 and 32 modes, it is almost complimentary, with 21 covering most of the range between $(\pi/4, 3\pi/4)$ and 32 covering the rest. Similarly, for $M=200 M_{\odot}$, (2,1), (3,2), and (4,3) modes cover different regions of parameter space. It can also be seen that as the total mass is increased, the contours include a larger region of the parameter space. The bi- and tri-modality of these contours reflect the symmetries these modes possess with respect to change in ι .

C. Detecting higher modes of GWTC-2 events using 3G detectors

Next, we investigate the detectability of higher modes for a few selected GWTC-2 catalog events assuming the sensitivity of 3G detectors. This helps us assess the improved detection rates that can be expected due to the use of an advanced detector configuration over what we already have from the present detectors. For this, we have chosen a few representative events from the

GWTC-2 catalog [3] with high detection significance, either because higher modes have already been detected for them by the LIGO-Virgo observations (GW190814, GW190412), or because the inclusion of higher modes in the waveform significantly improved the parameter estimation of the events [2].

Again, in this analysis, we consider the SNRs corresponding to a single CE detector placed at the location L (see Table I). For each event, in order to compute the distribution of SNRs for different higher order modes, we take 10,000 random posterior samples from the corresponding data-set available for that event. (see Ref. [3] for complete data-sets). We then take the median value of SNR from this distribution of 10,000 points and quote this value for each mode in Table II. Since we consider the minimum SNR value of 5 for this table, we have omitted the values for which SNRs were less than 5.

As expected, there is a significant improvement in the detection rate of higher modes as compared to the aLIGO and Virgo with their current sensitivities. The single 3G detector shows promise of detecting 33 and 44 modes for all of the above-mentioned events. Furthermore, 21 and 32 modes may also be detected in a few events. It is noteworthy that GW190814 shows the highest SNR values for the higher modes, as well as the highest relative SNR for 33 mode. This can clearly be explained by the high mass ratio value ($q \sim 9$) of this event. The 33 mode network SNR reported by LIGO-Virgo for this event was ~ 6.6 , whereas we can see that for a single CE detector, this number becomes ~ 170 . Similarly, the rel-

Event	M	q	χ_{eff}	SNR in mode				
				22	33	44	21	32
GW190412	42.6	3.2	0.2	649	81	17	14	-
GW190519_153544	159.5	1.6	0.4	685	79	48	19	14
GW190521	279.8	1.4	0.1	424	22	19	7.1	7.5
GW190602_175927	173.8	1.4	0.1	330	15	9.4	-	-
GW190630_185205	69.9	1.5	0.1	708	31	14	7.9	5.8
GW190706_222641	183.5	1.7	0.3	223	18	7.6	-	-
GW190814	27.2	9.0	0	982	172	33	32	-
GW190828_065509	44.4	2.4	0.1	418	34	7.2	6.7	-

Table II: Detectability of higher modes in GWTC-2 events using a 3G detector. The values quoted above are those for which the SNR > 5 . The blank spaces in the table denote SNR < 5 , hence those numbers have not been quoted. We have sampled the parameter values from the posteriors of these events[2, 3, 65, 66, 79], and have quoted the median values of SNRs obtained from 10,000 posterior samples. The total mass values quoted above are the detector frame masses.

ative contribution of higher modes is considerable (by a factor larger than 20) for GW190412. Such high SNR can be attributed to the event’s mass ratio ($q \sim 3.2$) and non-zero effective spin.

To summarize, several of the GWTC-2 events would have led to reliable detection of all the four leading modes of gravitational waveforms with the sensitivities of the proposed 3G detectors. However, a robust method to quantify the detectability of higher modes must involve synthesizing a population based on the inferences from the LIGO/Virgo detections so far. This forms the theme for the next section.

IV. POPULATION STUDY

Our knowledge of the BBH population in the universe has evolved from the first observing run through the first half of the third observing run of the LIGO/Virgo detectors. Here, we employ the state-of-the-art population model of Ref. [13] to synthesize a BBH population and assess the detectability of various sub-dominant modes by using the method introduced earlier.

As the 3G detectors will have significantly better low-frequency sensitivity compared to their 2G counterparts, they are excellent tools to detect intermediate-mass BBHs with total masses above $500M_{\odot}$. The inferences from GWTC-2 are based on black holes with a maximum total mass of about $150M_{\odot}$. Hence, in order to model the high mass regime, besides the GWTC-2 model, we consider an ‘extended model’ of the population by extrapolating the properties of the GWTC-2 population to higher mass BBHs. Admittedly, this is somewhat arbitrary. However, in the absence of any reliable model for the population of intermediate-mass BBHs, we use this model to assess the capabilities of 3G detectors to detect higher modes. These two models will be referred to as GWTC-2 and GWTC-2E, respectively, in the discus-

sions that follow.⁵ The details of these populations are discussed next.

A. Population models

For the GWTC-2 population, we closely follow [13] and consider the POWER LAW + PEAK model for total mass and mass ratio. The mass ratio (q) distribution is taken as q^{β} . Further details for this model can be found in Appendix B of Abbott et al. [13]. We also performed the analysis using BROKEN POWER LAW model and found results are in good agreement with the POWER LAW + PEAK model. For ease of presentation, we show results only for the latter.

To construct the ‘extended’ GWTC-2 population (or GWTC-2E), we extend the maximum total mass from $150M_{\odot}$ to $1000M_{\odot}$, anticipating the observations of such intermediate-mass binary black holes in the 3G detectors. The distribution for secondary mass component m_2 is taken to be uniform in the same range as m_1 . The mass ratio distribution has been taken up to the value $q_{\text{max}}=18$, which is the maximum q up to which the waveforms used here are calibrated [41].

For the spin distribution, we chose the DEFAULT MODEL. The distribution for dimensionless spin magnitude ($\chi_{1,2}$) in this model is given by,

$$p(\chi) = \text{Beta}(\alpha_{\chi}, \beta_{\chi}). \quad (9)$$

The mean (μ_{χ}) and variance (σ_{χ}^2) for the Beta distribution are used to calculate the values of α_{χ} and β_{χ} . We found these values to be: $\alpha_{\chi} = 1.3125$ and $\beta_{\chi} = 3.9375$, which were then implemented for the construction of the distribution for dimensionless spin magnitudes ($\chi_{1,2}$). Further the cosine of the tilt angle, defined as $z_{\chi} = \cos(\theta_{1,2})$, is distributed as $p(z_{\chi})$ (see Section D1 of Ref. [13] for related details). The distribution χ_{1z} and χ_{2z} reads

$$p(\chi_{1z,2z}) = p(\chi_{1z,2z}) p(z_{\chi}). \quad (10)$$

We have taken the same distribution for χ_{1z} and χ_{2z} , in the range $[-1,1]$.⁶ Spin distributions are the same for both GWTC-2 and the GWTC-2E populations.

We use the POWER-LAW redshift evolution model to distribute the sources in luminosity distance. The redshift distribution for this model is given by:

⁵The letter ‘E’ in ‘GWTC-2E’ signifies that an ‘extension’ of the population model based on GWTC-2 is considered.

⁶Note that the waveform we use (IMRPhenomHM) is calibrated up to spin magnitude of 0.85 (0.98 for equal mass systems), however, we have extended this up to 1 in order to include the complete range of spin magnitudes.

$$\frac{dN}{dz} = \frac{dV_c}{dz} (1+z)^{\kappa-1} \quad (11)$$

where V_c is the comoving volume and κ is the hyper-parameter with values $\kappa = 1.3$ (POWER LAW + PEAK model). We have used the standard expressions for dV_c/dz and the relations between redshift(z), comoving distance(D_c), and luminosity distance(D_L) [136]. In our population study, we distribute the sources starting at $D_L = 100$ Mpc up to a redshift of $z_{\text{max}}=2.3$ following [13].

The choice of the red-shift evolution model and of z_{max} is the same for GWTC-2E population too. Although intermediate-mass BBHs may be detected up to larger redshifts with 3G detectors, our lack of understanding of their redshift distribution compels us to make this likely conservative choice. This choice implies an SNR threshold of 25 for the GWTC-2 population and 15 for the GWTC-2E population.

B. SNR distribution of higher modes

Both for the GWTC-2 and the GWTC-2E population models, we simulate 10,000 sources following the above-mentioned prescription. We vary all the 9 parameters, the luminosity distance (D_L), inclination angle (ι), total mass (M), mass ratio (q), sky angles (θ, ϕ), orientation angle (ψ), and spins (χ_{1z} and χ_{2z}), following the population models. The ranges for the total mass, mass ratio, spins, and redshift have been mentioned with their respective population models in section IV A. The cosines of the angles ι and θ have been varied uniformly between $(-1, 1)$, and ϕ and ψ are uniform between $(0, 2\pi)$. It is worth mentioning that due to the low mass of the secondary, which falls in the NS-BH mass gap, GW190814 is an outlier. Thus, the O3a population models do not include it while calculating the hyperparameters [13]. Note however, while the O3a population model excludes GW190814 (based on low secondary mass), our choice of prior for mass-ratio bounded in the range $[1, 18]$ for the simulated populations (both GWTC-2 and GWTC-2E) will naturally include a representation of systems as asymmetric as GW190814.

1. Comparison between the results from GWTC-2 and GWTC-2E population models

Figure 3 shows the cumulative histograms for the SNRs of various modes in the LAE network of 3G detectors (see Sec. II B for details). The numbers in brackets are the median values of SNR for each mode. For a particular value of SNR (on the x-axis), the y-axis corresponds to the fraction of population having SNR up to that value. Since all the 10,000 sources have $\text{SNR} > 10$ in 22 mode, we can say that 100% of these sources will be detectable

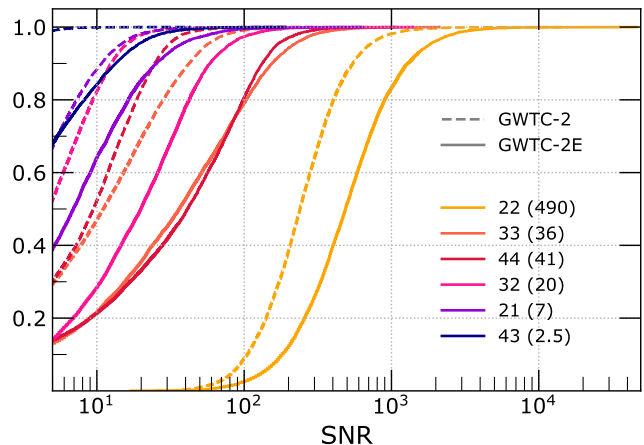


Figure 3: Cumulative histograms of SNR for various higher modes. The plot shows the trends for each mode between $\text{SNR}=5$ to maximum SNR reached by the 22 mode. The dashed lines denote the population drawn from the existing GWTC-2 catalog models keeping all the parameter ranges as quoted in the population paper. The solid coloured lines show the extension of mass model upto $M_{\text{max}} = 1000M_{\odot}$. The values written in the bracket are median values of SNR for each mode. The network taken is 3G LAE network.

at least in the quadrupolar mode. We have shown the results for two populations. It is worth recalling that the detectability criterion here is the SNR of a particular mode being at least 10.

The dashed lines correspond to the GWTC-2 population, while the solid lines correspond to the GWTC-2E population. The difference in detectability of HMs between these two populations is evident. The 33 and 44 modes are detectable in nearly 80% of the sources for the GWTC-2E population, whereas this number is only about 50% for the GWTC-2 population. The other modes are barely detectable for the GWTC-2 population whereas, for GWTC-2E, we see that 32 mode can be detected for nearly 70% of the sources. The 21 and 43 modes are also detectable in nearly 40% and 20% sources respectively. This increase in the detectable fraction is expected for the extended population since it contains more number of high mass binaries. These binaries increase the power in all the modes since higher mass contributes towards a higher amplitude of the signal. Also, high mass systems merge at lower frequencies and the 3G detectors are sensitive to the low frequencies, thus increasing the SNRs further.

2. Comparison between various generations of detector networks

In this section, we investigate how the detectability of higher modes changes for a population across various generations of detector networks. We consider 3 kinds of detector networks for this study: LIGO-A+, LIGO-

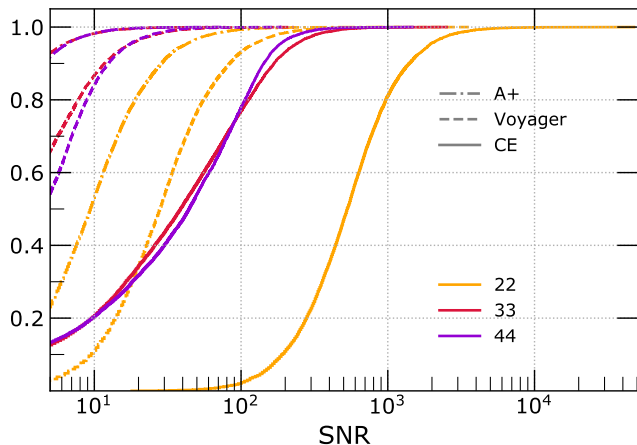


Figure 4: Cumulative histograms of SNR for various higher modes as a comparison between various generations of detectors. The solid coloured lines denote 3G detector network with CE, the dashed lines denote the detector network using LIGO Voyager, and the lines with dot-dashed style denote the detector network using LIGO A+. All the detectors have been placed at the locations of the LHV network. We have taken $M_{\text{max}} = 1000M_{\odot}$, $q_{\text{max}} = 18$.

Voyager, and CE detector networks. In order to avoid detector location bias, we have chosen the same set of locations, Livingston and Hanford in the US and Cascina in Italy (LHV) for all three networks.

We have shown the results in Fig. 4. Even a quick look at the Fig. 4 reveals that the LIGO A+ and LIGO Voyager detector networks can detect a maximum of two additional modes besides the quadrupole mode, whereas 3G detectors are expected to detect five of the non-quadrupolar modes. As expected, the improvement with 3G detectors is highly significant compared to the upgraded 2G configurations. While only 10-20% of sources allow the detection of 33 and 44 modes in the upgraded 2G network, the 3G network can detect as many as 80% of the population. This shows the tremendous potential of a network of a 3G detectors, and how the number of higher mode detections will significantly rise compared to the currently operating 2G detectors. This, in turn, will also have a profound impact on the overall parameter estimation capabilities of the 3G detectors, and hence influence the astrophysics and fundamental physics in the 3G era in a big way.

V. CONCLUSIONS

We have investigated the detectability of non-quadrupole modes of gravitational wave radiation mass ratio and inclination angle space (Section III B), and for a few events from the GWTC-2 catalog assuming as if they were detected during the 3G era (Section III C). We find that various modes activate different regions of the q - ι plane, and show various symmetries in ι lead-

ing to bi- and tri- modality in the contours. For the GWTC-2 events, we observe a massive improvement of SNR (by a factor larger than 20 times) for the events which had been reported to show detection in 33 mode by LIGO/Virgo observations (GW190814, GW190412). In the 3G era, events like these promise to show a detection in other higher harmonics as well. Apart from this, we also see detectable SNRs in higher modes for other GWTC-2 events, which emphasizes that the number of events that permit the measurement of higher modes will also increase in the 3G era.

We also performed a population study for 10,000 sources which will be detected by the 3G network, and quote the fraction of population which will show the presence of higher modes (Section IV B). It is found that nearly 80% of the sources will have detectable SNRs in 33 and 44 modes, and other modes will also be detectable in a small percentage of the population. Additionally, we compared this fraction with the fraction of higher modes detectable in the upgraded 2G gravitational wave detector networks such as LIGO A+ and LIGO Voyager. We conclude that this fraction significantly increases from less than 20% to nearly 80% for the 33 and 44 modes, with the 3G network.

All the above-mentioned investigations were performed using a spinning inspiral-merger-ringdown higher mode waveform of the Phenom family (IMRPhenomHM), and using a different waveform may alter the numbers only slightly. Effects of the mass ratio and inclination angle were observed in the detectability of higher order modes. The effect of increasing total mass (in discrete values) was also noted in Section III B. While we have shown the detectability of various modes for spinning systems, a more detailed study can be done by including the effect of precession along with the higher modes. Further, as a follow-up, we plan to explore the effect of higher modes in the error analysis of various parameters in the 3G detector era.

Acknowledgments

We thank Ajit Mehta for the review of our manuscript and for offering useful comments. We thank B.S. Sathyaprakash and Anuradha Gupta for useful conversations. We are grateful to Ssohrab Borhanian, Sumit Kumar, and Collin Capano for their help with the antenna pattern functions. We thank Sebastian Khan for clarifications on the waveform. We acknowledge the help from users on ‘pycbc-help slack channel’ in implementing the PyCBC code. K.G.A. is partially supported by a grant from the Infosys Foundation. K.G.A. acknowledges the Swarnajayanti grant DST/SJF/PSA-01/2017-18 of DST-India, the Core Research Grant EMR/2016/005594, and MATRICS grant MTR/2020/000177 of SERB. The population studies reported in this paper were carried out using the Powehi workstation in the Department of Physics, and AQUA cluster at IIT Madras.

-
- [1] B. Abbott et al. (LIGO Scientific, Virgo), *Phys. Rev. Lett.* **116**, 061102 (2016), arXiv:1602.03837.
- [2] R. Abbott et al. (LIGO Scientific, Virgo) (2020), arXiv:2010.14527.
- [3] LIGO Scientific Collaboration and Virgo Collaboration, (2020), URL <https://www.gw-openscience.org/eventapi/html/GWTC/>.
- [4] J. M. Antelis and C. Moreno, *Gen. Rel. Grav.* **51**, 61 (2019), arXiv:1807.07660.
- [5] T. Venumadhav, B. Zackay, J. Roulet, L. Dai, and M. Zaldarriaga, *Phys. Rev. D* **100**, 023011 (2019), arXiv:1902.10341.
- [6] T. Venumadhav, B. Zackay, J. Roulet, L. Dai, and M. Zaldarriaga, *Phys. Rev. D* **101**, 083030 (2020), arXiv:1904.07214.
- [7] A. H. Nitz, C. Capano, A. B. Nielsen, S. Reyes, R. White, D. A. Brown, and B. Krishnan, *Astrophys. J.* **872**, 195 (2019), arXiv:1811.01921.
- [8] A. H. Nitz, T. Dent, G. S. Davies, S. Kumar, C. D. Capano, I. Harry, S. Mozzon, L. Nuttall, A. Lundgren, and M. Tápai, *Astrophys. J.* **891**, 123 (2020), arXiv:1910.05331.
- [9] B. P. Abbott et al. (LIGO Scientific, Virgo), *Astrophys. J. Lett.* **818**, L22 (2016), arXiv:1602.03846.
- [10] B. P. Abbott et al. (LIGO Scientific, Virgo, Fermi GBM, INTEGRAL, IceCube, AstroSat Cadmium Zinc Telluride Imager Team, IPN, Insight-Hxmt, ANTARES, Swift, AGILE Team, 1M2H Team, Dark Energy Camera GW-EM, DES, DLT40, GRAWITA, Fermi-LAT, ATCA, ASKAP, Las Cumbres Observatory Group, OzGrav, DWF (Deeper Wider Faster Program), AST3, CAASTRO, VINROUGE, MASTER, J-GEM, GROWTH, JAGWAR, CaltechNRAO, TTU-NRAO, NuSTAR, Pan-STARRS, MAXI Team, TZAC Consortium, KU, Nordic Optical Telescope, ePESSTO, GROND, Texas Tech University, SALT Group, TOROS, BOOTES, MWA, CALET, IKI-GW Follow-up, H.E.S.S., LOFAR, LWA, HAWC, Pierre Auger, ALMA, Euro VLBI Team, Pi of Sky, Chandra Team at McGill University, DFN, ATLAS Telescopes, High Time Resolution Universe Survey, RIMAS, RATIR, SKA South Africa/MeerKAT), *Astrophys. J. Lett.* **848**, L12 (2017), arXiv:1710.05833.
- [11] B. P. Abbott et al. (LIGO Scientific, Virgo, 1M2H, Dark Energy Camera GW-E, DES, DLT40, Las Cumbres Observatory, VINROUGE, MASTER), *Nature* **551**, 85 (2017), arXiv:1710.05835.
- [12] R. Abbott et al. (LIGO Scientific, Virgo) (2020), arXiv:2010.14529.
- [13] R. Abbott et al. (LIGO Scientific, Virgo) (2020), arXiv:2010.14533.
- [14] J. Aasi et al. (LIGO Scientific), *Class. Quant. Grav.* **32**, 074001 (2015), arXiv:1411.4547.
- [15] F. Acernese (Virgo), *J. Phys. Conf. Ser.* **610**, 012014 (2015).
- [16] T. Akutsu et al. (KAGRA) (2020), arXiv:2005.05574.
- [17] D. Shoemaker (LIGO Scientific) (2019), arXiv:1904.03187.
- [18] D. McClelland, M. Evans, R. Schnabel, B. Lantz, I. Martin, and V. Quetschke (2016), URL <https://dcc.ligo.org/LIGO-T1500290/public>.
- [19] M. Punturo et al., *Class. Quant. Grav.* **27**, 194002 (2010).
- [20] S. Dwyer, D. Sigg, S. W. Ballmer, L. Barsotti, N. Mavalvala, and M. Evans, *Phys. Rev. D* **91**, 082001 (2015), arXiv:1410.0612.
- [21] B. P. Abbott et al. (LIGO Scientific), *Class. Quant. Grav.* **34**, 044001 (2017), arXiv:1607.08697.
- [22] S. Hild et al., *Class. Quant. Grav.* **28**, 094013 (2011), arXiv:1012.0908.
- [23] K. Chamberlain and N. Yunes, *Phys. Rev. D* **96**, 084039 (2017), arXiv:1704.08268.
- [24] K. S. Thorne, in *Three hundred years of gravitation*, edited by S. Hawking and W. Israel (Cambridge University Press, 1987), pp. 330–458.
- [25] C. Helström, *Statistical Theory of Signal Detection*, vol. 9 of *International Series of Monographs in Electronics and Instrumentation* (Pergamon Press, Oxford, U.K., New York, U.S.A., 1968), 2nd ed.
- [26] L. Blanchet, *Living Rev. Rel.* **17**, 2 (2014), arXiv:1310.1528.
- [27] N. T. Bishop and L. Rezzolla, *Living Rev. Rel.* **19**, 2 (2016), arXiv:1606.02532.
- [28] M. Sasaki and H. Tagoshi, *Living Rev. Rel.* **6**, 6 (2003), arXiv:gr-qc/0306120.
- [29] P. Ajith et al., *Class. Quant. Grav.* **24**, S689 (2007), arXiv:0704.3764.
- [30] A. Buonanno and T. Damour, *Phys. Rev. D* **62**, 064015 (2000), arXiv:gr-qc/0001013.
- [31] E. Poisson, A. Pound, and I. Vega, *Living Rev. Rel.* **14**, 7 (2011), arXiv:1102.0529.
- [32] S. Foffa and R. Sturani, *Class. Quant. Grav.* **31**, 043001 (2014), arXiv:1309.3474.
- [33] H. Tagoshi, C. K. Mishra, A. Pai, and K. Arun, *Phys. Rev. D* **90**, 024053 (2014), arXiv:1403.6915.
- [34] V. Varma, P. Ajith, S. Husa, J. C. Bustillo, M. Hannam, and M. Pürrer, *Phys. Rev. D* **90**, 124004 (2014), arXiv:1409.2349.
- [35] V. Varma and P. Ajith, *Phys. Rev. D* **96**, 124024 (2017), arXiv:1612.05608.
- [36] C. Kalaghatgi, M. Hannam, and V. Raymond, *Phys. Rev. D* **101**, 103004 (2020), arXiv:1909.10010.
- [37] E. Payne, C. Talbot, and E. Thrane, *Phys. Rev. D* **100**, 123017 (2019), arXiv:1905.05477.
- [38] J. Lange, R. O’Shaughnessy, and M. Rizzo (2018), arXiv:1805.10457.
- [39] A. K. Mehta, C. K. Mishra, V. Varma, and P. Ajith, *Phys. Rev. D* **96**, 124010 (2017), arXiv:1708.03501.
- [40] A. Kumar Mehta, P. Tiwari, N. K. Johnson-McDaniel, C. K. Mishra, V. Varma, and P. Ajith, *Phys. Rev. D* **100**, 024032 (2019), arXiv:1902.02731.
- [41] L. London, S. Khan, E. Fauchon-Jones, C. García, M. Hannam, S. Husa, X. Jiménez-Forteza, C. Kalaghatgi, F. Ohme, and F. Pannarale, *Phys. Rev. Lett.* **120**, 161102 (2018), arXiv:1708.00404.
- [42] S. Khan, K. Chatziioannou, M. Hannam, and F. Ohme, *Phys. Rev. D* **100**, 024059 (2019), arXiv:1809.10113.
- [43] S. Khan, F. Ohme, K. Chatziioannou, and M. Hannam, *Phys. Rev. D* **101**, 024056 (2020), arXiv:1911.06050.
- [44] R. Cotesta, A. Buonanno, A. Bohé, A. Taracchini, I. Hinder, and S. Ossokine, *Phys. Rev. D* **98**, 084028 (2018), arXiv:1803.10701.

- [45] R. Cotesta, S. Marsat, and M. Pürrer, *Phys. Rev. D* **101**, 124040 (2020), arXiv:2003.12079.
- [46] C. Van Den Broeck and A. S. Sengupta, *Class. Quant. Grav.* **24**, 155 (2007), arXiv:gr-qc/0607092.
- [47] K. Arun, B. R. Iyer, B. Sathyaprakash, and S. Sinha, *Phys. Rev. D* **75**, 124002 (2007), arXiv:0704.1086.
- [48] C. Van Den Broeck and A. S. Sengupta, *Class. Quant. Grav.* **24**, 1089 (2007), arXiv:gr-qc/0610126.
- [49] K. Arun, A. Buonanno, G. Faye, and E. Ochsner, *Phys. Rev. D* **79**, 104023 (2009), [Erratum: *Phys. Rev. D* **84**, 049901 (2011)], arXiv:0810.5336.
- [50] S. A. Usman, J. C. Mills, and S. Fairhurst, *Astrophys. J.* **877**, 82 (2019), arXiv:1809.10727.
- [51] F. Ohme, A. B. Nielsen, D. Keppel, and A. Lundgren, *Phys. Rev. D* **88**, 042002 (2013), arXiv:1304.7017.
- [52] M. Hannam, D. A. Brown, S. Fairhurst, C. L. Fryer, and I. W. Harry, *Astrophys. J. Lett.* **766**, L14 (2013), arXiv:1301.5616.
- [53] K. Arun, B. R. Iyer, B. Sathyaprakash, S. Sinha, and C. Van Den Broeck, *Phys. Rev. D* **76**, 104016 (2007), [Erratum: *Phys. Rev. D* **76**, 129903 (2007)], arXiv:0707.3920.
- [54] M. Trias and A. M. Sintes, *Phys. Rev. D* **77**, 024030 (2008), arXiv:0707.4434.
- [55] S. Babak, M. Hannam, S. Husa, and B. F. Schutz, (2008), arXiv:0806.1591.
- [56] K. Arun, H. Tagoshi, C. K. Mishra, and A. Pai, *Phys. Rev. D* **90**, 024060 (2014), arXiv:1403.6917.
- [57] R. O’Shaughnessy, B. Farr, E. Ochsner, H.-S. Cho, V. Raymond, C. Kim, and C.-H. Lee, *Phys. Rev. D* **89**, 102005 (2014), arXiv:1403.0544.
- [58] P. B. Graff, A. Buonanno, and B. S. Sathyaprakash, *Phys. Rev. D* **92**, 022002 (2015), arXiv:1504.04766.
- [59] J. Calderón Bustillo, S. Husa, A. M. Sintes, and M. Pürrer, *Phys. Rev. D* **93**, 084019 (2016), arXiv:1511.02060.
- [60] J. Calderón Bustillo, P. Laguna, and D. Shoemaker, *Phys. Rev. D* **95**, 104038 (2017), arXiv:1612.02340.
- [61] P. Kumar, J. Blackman, S. E. Field, M. Scheel, C. R. Galley, M. Boyle, L. E. Kidder, H. P. Pfeiffer, B. Szilágyi, and S. A. Teukolsky, *Phys. Rev. D* **99**, 124005 (2019), arXiv:1808.08004.
- [62] K. Chatziioannou et al., *Phys. Rev. D* **100**, 104015 (2019), arXiv:1903.06742.
- [63] F. H. Shaik, J. Lange, S. E. Field, R. O’Shaughnessy, V. Varma, L. E. Kidder, H. P. Pfeiffer, and D. Wysocki, *Phys. Rev. D* **101**, 124054 (2020), arXiv:1911.02693.
- [64] M. Pürrer and C.-J. Haster, *Phys. Rev. Res.* **2**, 023151 (2020), arXiv:1912.10055.
- [65] R. Abbott et al. (LIGO Scientific, Virgo), *Phys. Rev. D* **102**, 043015 (2020), arXiv:2004.08342.
- [66] R. Abbott et al. (LIGO Scientific, Virgo), *Astrophys. J. Lett.* **896**, L44 (2020), arXiv:2006.12611.
- [67] S. Borhanian, A. Dhani, A. Gupta, K. Arun, and B. Sathyaprakash, *Astrophys. J. Lett.* **905**, L28 (2020), arXiv:2007.02883.
- [68] B. Sathyaprakash, B. Schutz, and C. Van Den Broeck, *Class. Quant. Grav.* **27**, 215006 (2010), arXiv:0906.4151.
- [69] C. K. Mishra, K. Arun, B. R. Iyer, and B. Sathyaprakash, *Phys. Rev. D* **82**, 064010 (2010), arXiv:1005.0304.
- [70] N. Yunes and F. Pretorius, *Phys. Rev. D* **80**, 122003 (2009), arXiv:0909.3328.
- [71] K. Arun and C. M. Will, *Class. Quant. Grav.* **26**, 155002 (2009), arXiv:0904.1190.
- [72] S. Dhanpal, A. Ghosh, A. K. Mehta, P. Ajith, and B. Sathyaprakash, *Phys. Rev. D* **99**, 104056 (2019), arXiv:1804.03297.
- [73] T. Islam, A. K. Mehta, A. Ghosh, V. Varma, P. Ajith, and B. Sathyaprakash, *Phys. Rev. D* **101**, 024032 (2020), arXiv:1910.14259.
- [74] C. D. Capano and A. H. Nitz, *Phys. Rev. D* **102**, 124070 (2020), arXiv:2008.02248.
- [75] S. Kastha, A. Gupta, K. G. Arun, B. S. Sathyaprakash, and C. Van Den Broeck, *Phys. Rev. D* **98**, 124033 (2018), arXiv:1809.10465.
- [76] S. Kastha, A. Gupta, K. G. Arun, B. S. Sathyaprakash, and C. Van Den Broeck, *Phys. Rev. D* **100**, 044007 (2019), arXiv:1905.07277.
- [77] S. J. Kapadia, M. K. Singh, M. A. Shaikh, D. Chatterjee, and P. Ajith, *Astrophys. J. Lett.* **898**, L39 (2020), arXiv:2005.08830.
- [78] M. K. Singh, S. J. Kapadia, M. A. Shaikh, D. Chatterjee, and P. Ajith (2020), arXiv:2010.12407.
- [79] R. Abbott et al. (LIGO Scientific, Virgo), *Phys. Rev. Lett.* **125**, 101102 (2020), arXiv:2009.01075.
- [80] K. Thorne, *Rev. Mod. Phys.* **52**, 299 (1980).
- [81] L. E. Kidder, *Phys. Rev. D* **77**, 044016 (2008), arXiv:0710.0614.
- [82] L. Blanchet, G. Faye, B. R. Iyer, and S. Sinha, *Class. Quant. Grav.* **25**, 165003 (2008), [Erratum: *Class. Quant. Grav.* **29**, 239501 (2012)], arXiv:0802.1249.
- [83] A. H. Mroue et al., *Phys. Rev. Lett.* **111**, 241104 (2013), arXiv:1304.6077.
- [84] J. Goldberg, A. MacFarlane, E. Newman, F. Rohrlich, and E. Sudarshan, *J. Math. Phys.* **8**, 2155 (1967).
- [85] J. Blackman, S. E. Field, M. A. Scheel, C. R. Galley, C. D. Ott, M. Boyle, L. E. Kidder, H. P. Pfeiffer, and B. Szilágyi, *Phys. Rev. D* **96**, 024058 (2017), arXiv:1705.07089.
- [86] V. Varma, S. E. Field, M. A. Scheel, J. Blackman, L. E. Kidder, and H. P. Pfeiffer, *Phys. Rev. D* **99**, 064045 (2019), arXiv:1812.07865.
- [87] V. Varma, S. E. Field, M. A. Scheel, J. Blackman, D. Gerosa, L. C. Stein, L. E. Kidder, and H. P. Pfeiffer, *Phys. Rev. Research* **1**, 033015 (2019), arXiv:1905.09300.
- [88] N. E. Rifat, S. E. Field, G. Khanna, and V. Varma, *Phys. Rev. D* **101**, 081502 (2020), arXiv:1910.10473.
- [89] A. Nagar, G. Riemenschneider, G. Pratten, P. Rettegno, and F. Messina, *Phys. Rev. D* **102**, 024077 (2020), arXiv:2001.09082.
- [90] C. García-Quirós, M. Colleoni, S. Husa, H. Estellés, G. Pratten, A. Ramos-Buades, M. Mateu-Lucena, and R. Jaume, *Phys. Rev. D* **102**, 064002 (2020), arXiv:2001.10914.
- [91] S. Ossokine et al., *Phys. Rev. D* **102**, 044055 (2020), arXiv:2004.09442.
- [92] G. Pratten et al. (2020), arXiv:2004.06503.
- [93] A. Nagar, P. Rettegno, R. Gamba, and S. Bernuzzi (2020), arXiv:2009.12857.
- [94] F. Foucart et al. (2020), arXiv:2010.14518.
- [95] A. Nagar, A. Bonino, and P. Rettegno (2021), arXiv:2101.08624.
- [96] X. Liu, Z. Cao, and Z.-H. Zhu (2021), arXiv:2102.08614.
- [97] LIGO Scientific Collaboration, *LIGO Algorithm Library - LALSuite*, free software

- (GPL) (2018), URL <https://lscsoft.docs.ligo.org/lalsuite/lalsimulation/>.
- [98] L. Blanchet, T. Damour, B. R. Iyer, C. M. Will, and A. G. Wiseman, Phys. Rev. Lett. **74**, 3515 (1995), arXiv:gr-qc/9501027.
 - [99] L. Blanchet, T. Damour, and B. R. Iyer, Phys. Rev. D **51**, 5360 (1995), arXiv:gr-qc/9501029.
 - [100] L. Blanchet, Phys. Rev. D **54**, 1417 (1996), Erratum-ibid. **71**, 129904(E) (2005), arXiv:gr-qc/9603048.
 - [101] L. Blanchet, B. R. Iyer, and B. Joguet, Phys. Rev. D **65**, 064005 (2002), Erratum-ibid **71**, 129903(E) (2005), arXiv:gr-qc/0105098.
 - [102] L. Blanchet, G. Faye, B. R. Iyer, and B. Joguet, Phys. Rev. D **65**, 061501(R) (2002), Erratum-ibid **71**, 129902(E) (2005), arXiv:gr-qc/0105099.
 - [103] L. Blanchet, T. Damour, G. Esposito-Farèse, and B. R. Iyer, Phys. Rev. Lett. **93**, 091101 (2004), arXiv:gr-qc/0406012.
 - [104] L. Blanchet, B. R. Iyer, C. M. Will, and A. G. Wiseman, Class. Quantum Grav. **13**, 575 (1996), arXiv:gr-qc/9602024.
 - [105] K. Arun, L. Blanchet, B. R. Iyer, and M. S. Qusailah, Class. Quant. Grav. **21**, 3771 (2004), [Erratum: Class. Quant. Grav. **22**, 3115 (2005)], arXiv:gr-qc/0404085.
 - [106] L. E. Kidder, Phys. Rev. D **52**, 821 (1995), arXiv:gr-qc/9506022.
 - [107] L. Blanchet, A. Buonanno, and G. Faye, Phys. Rev. D **74**, 104034 (2006), erratum-ibid. **75**, 049903 (E) (2007), arXiv:gr-qc/0605140.
 - [108] R. A. Porto and I. Z. Rothstein, Phys. Rev. D **78**, 044013 (2008), [Erratum: Phys. Rev. D **81**, 029905 (2010)], arXiv:0804.0260.
 - [109] R. A. Porto and I. Z. Rothstein, Phys. Rev. D **78**, 044012 (2008), [Erratum: Phys. Rev. D **81**, 029904 (2010)], arXiv:0802.0720.
 - [110] R. A. Porto, A. Ross, and I. Z. Rothstein, JCAP **03**, 009 (2011), arXiv:1007.1312.
 - [111] S. Marsat, A. Bohe, G. Faye, and L. Blanchet, Class. Quant. Grav. **30**, 055007 (2013), arXiv:1210.4143.
 - [112] A. Bohe, S. Marsat, G. Faye, and L. Blanchet, Class. Quant. Grav. **30**, 075017 (2013), arXiv:1212.5520.
 - [113] A. Buonanno, G. Faye, and T. Hinderer, Phys. Rev. D **87**, 044009 (2013), arXiv:1209.6349.
 - [114] S. Marsat, A. Bohé, L. Blanchet, and A. Buonanno, Class. Quant. Grav. **31**, 025023 (2014), arXiv:1307.6793.
 - [115] C. K. Mishra, A. Kela, K. Arun, and G. Faye, Phys. Rev. D **93**, 084054 (2016), arXiv:1601.05588.
 - [116] A. Buonanno and T. Damour, Phys. Rev. D **59**, 084006 (1999), arXiv:gr-qc/9811091.
 - [117] T. Damour, P. Jaranowski, and G. Schaefer, Phys. Rev. D **62**, 084011 (2000), arXiv:gr-qc/0005034.
 - [118] T. Damour, Phys. Rev. D **64**, 124013 (2001), arXiv:gr-qc/0103018.
 - [119] T. Damour, P. Jaranowski, and G. Schäfer, Phys. Rev. D **91**, 084024 (2015), arXiv:1502.07245.
 - [120] W. D. Goldberger and I. Z. Rothstein, Phys. Rev. D **73**, 104029 (2006), arXiv:hep-th/0409156.
 - [121] N. Sennett, R. Brito, A. Buonanno, V. Gorbenko, and L. Senatore, Phys. Rev. D **102**, 044056 (2020), arXiv:1912.09917.
 - [122] M. Boyle et al., Class. Quant. Grav. **36**, 195006 (2019), arXiv:1904.04831.
 - [123] K. Jani, J. Healy, J. A. Clark, L. London, P. Laguna, and D. Shoemaker, Class. Quant. Grav. **33**, 204001 (2016), arXiv:1605.03204.
 - [124] B. Bruegmann, J. A. Gonzalez, M. Hannam, S. Husa, U. Sperhake, and W. Tichy, Phys. Rev. D **77**, 024027 (2008), arXiv:gr-qc/0610128.
 - [125] P. Ajith et al., Class. Quant. Grav. **29**, 124001 (2012), [Erratum: Class. Quant. Grav. **30**, 199401 (2013)], arXiv:1201.5319.
 - [126] I. Hinder et al., Class. Quant. Grav. **31**, 025012 (2014), arXiv:1307.5307.
 - [127] S. Borhanian (2020), arXiv:2010.15202.
 - [128] LIGO gitlab, URL <https://git.ligo.org/evan.hall/gw-horizon-plot/-/blob/master/data/voyager.dat>.
 - [129] C. Cutler et al., Phys. Rev. Lett. **70**, 2984 (1993), arXiv:astro-ph/9208005.
 - [130] C. Cutler and E. E. Flanagan, Phys. Rev. D **49**, 2658 (1994), arXiv:gr-qc/9402014.
 - [131] Y. Wiaux, L. Jacques, and P. Vandergheynst, J. Comput. Phys. **226**, 2359 (2007), arXiv:astro-ph/0508514.
 - [132] C. Mills and S. Fairhurst (2020), arXiv:2007.04313.
 - [133] S. Ghonge, K. Chatziioannou, J. A. Clark, T. Littenberg, M. Millhouse, L. Cadonati, and N. Cornish, Phys. Rev. D **102**, 064056 (2020), arXiv:2003.09456.
 - [134] S. Roy, A. S. Sengupta, and K. G. Arun (2019), arXiv:1910.04565.
 - [135] B. D. O'Brien, C. F. Da Silva Costa, and S. Klimenko (2019), arXiv:1901.09072.
 - [136] D. W. Hogg (1999), arXiv:astro-ph/9905116.